INTERNATIONAL JOURNAL FOR NUMERICAL METHODS IN FLUIDS
Int. J. Numer. Meth. Fluids 2002; **39**:301–324 (DOI: 10.1002/fld.327)

Thin-tube vortex simulations for sinusoidal instability in a counter-rotating vortex pair

Z. C. Zheng*,†

Department of Mechanical and Nuclear Engineering, Kansas State University, Manhattan, Kansas 66506-5205, U.S.A.

SUMMARY

A thin-tube vortex method is developed to investigate the intrinsic instability within a counter-rotating vortex pair system and the effects from the core size and the wavenumbers (or wavelengths). The numerical accuracy and the advantages of the scheme are theoretically estimated. A nearest-neighbour-image method is employed in this three-dimensional vortex simulation. Agreement with Crow's instability analysis has been achieved numerically for the long-wave cases. A short-wave instability for the zeroth radial mode of bending instability has also been found using the thin-tube vortex simulations. Then, the combinations of long- and short-wave instability are investigated to elucidate the non-linear effects due to the interactions of two different modes. It is shown that instability is enhanced if both long- and short-wave instabilities occur simultaneously. Although the method used in the paper is not capable of including effects such as axial flow, vortex core deformation and other complicated viscous effects, it effectively predicts and clarifies the first-order factor that dominates the sinusoidal instability behaviour in a vortex pair. Copyright © 2002 John Wiley & Sons, Ltd.

KEY WORDS: vortex methods; vortex instability; sinusoidal waves

1. INTRODUCTION

Sinusoidal instabilities can be found, at various length scales, from coherent structures in turbulence to aircraft wake vortices. In his well-known paper, Crow [1] investigated the mutual and self-inductions under small perturbations in a pair of trailing vortices, using small core (relative to the unperturbed vortex pair spacing), long-wave (relative to the vortex core size) assumptions and linear stability analysis. The occurrence of sinusoidal instability (also sometimes called the Crow instability after Crow) depends on the balance between the straining effects from mutual induction and the stabilizing effects from self-induction. The stability diagrams developed in that study have been used as criteria for the Crow instability. Although both long-wave and short-wave instabilities are shown in Crow's analysis, it was pointed out

*Correspondence to: Z. C. Zheng, Department of Mechanical and Nuclear Engineering, Kansas State University, Manhattan, Kansas 66506-5205, U.S.A.
†E-mail: zzheng@ksu.edu

later by Widnall *et al.* [2] that the short-wave results are spurious, because of the wavelength limit.

Moore [3] extended the criteria for the symmetric mode to finite amplitude waves and found that Crow's results were applicable nearly up to the point at which the two vortices touched. Leonard [4] used a vortex filament method to simulate an aircraft trailing vortex pair, which was perturbed with a small random perturbation having a Kolmogoroff energy spectrum. The Crow instability under atmospheric turbulence conditions has been studied by many researchers, e.g., analytically by Crow and Bate [5], experimentally by Sarpkaya and Daly [6] and, more recently, numerically by Spalart and Wray [7], Han *et al.* [8], Robins and Delisi [9] and Zheng and Baek [10].

Thomas and Auerbach [11] observed the simultaneous development of a long- and a short-wave instability mode in a vortex pair. The long wavelengths are in good agreement with the classical symmetric long-wave bending mode identified by Crow [1]. The developing short waves appear to be less accurately described by the theoretical results by Widnall *et al.* [2]. Leweke and Williamson [12] investigated the instability to short waves of the order of the vortex core size. They identified this phenomenon as a manifestation of an elliptic instability of the vortex cores. Orlandi *et al.* [13] used direct numerical simulations (DNS) to reproduce results of the laboratory measurements by Leweke and Williamson [12]. Klein and Majda [14] derived an asymptotic theory describing the non-linear dynamics of perturbed vortex pairs. In contrast to linear theory, they found that in the non-linear regime of interaction, small antisymmetric perturbations could have a dramatic effect on symmetric solutions. A superimposed small antisymmetric perturbation accelerated the nonlinear energy transfer significantly and led to an earlier critical solution with asymmetric behaviour.

There is rich literature on vortex ring sinusoidal instability which is related to vortex pair instability. However, they are not discussed for the purpose of the topic covered in this paper. Readers are referred to the papers by Shariff *et al.* [15] and Shariff and Leonard [16].

In this paper, a thin-tube vortex method with Rosenhead [17] core has been developed to simulate the motion of a vortex pair undergoing sinusoidal disturbances. The construction of a three-dimensional vortex filament model starts with discretization of a slender vortex into a finite number of vortex elements. If only one numerical filament is used instead of a collection of overlapping numerical filaments to approximate the vorticity field of one continuous vortex structure, the resulting method is called the thin-tube vortex filament method [18]. A constant circulation along the filament is specified according to Kelvin and Helmholtz. In the method used here, the core size is constant throughout the filament and does not change with time, since conservation of vorticity volume is not required. Therefore, the filament vorticity changes only due to local stretching and tilting of each vortex element. In this way, the vorticity transport equation is implicitly accounted for [19].

In the developed numerical scheme, the vortex filament is discretized into straight-line segments. Exact integrations are performed on each segment. The only error source during this procedure is generated by using a straight line to approximate each vortex segment which is a three-dimensional curve in general. If vortex stretching happens, the relative curvature is reduced which can compensate for the errors due to longer segment lengths, thus no points need to be added to reduce the error. On the other hand, when the vortex shrinking occurs, the number of points automatically increases in the shrinking region to reduce the errors caused by curvature effects due to the straight-line approximation for the vortex segment.

Periodicity in the axial direction of the vortex pair is another character of this problem. The convective nature of the vortex pair prevents finite periodic image truncations in the calculation, since non-physical end effects increase with time. Strictly speaking, the Biot–Savart evaluation of the velocity requires integration over all the periodic images in the flowfield. Moore [3], Klein and Knio [19] and Wang [18] developed techniques to precalculate the functions related to periodic images for discrete values using a large number of cut-off images. In the following calculation, a nearest-neighbour-image method [20, 21] has been implemented to reduce the end effects caused by the finite periodic images in the three-dimensional vortex method. This approach has been proved to be effective in calculating periodic flow without being restricted to the format of the precalculated functions.

It should be pointed out that the algorithm developed in this study is not capable of including effects such as axial flow, vortex core deformation and other complicated viscous effects which, the author agrees, are stringent issues in vortex dynamics. However, while unsteady three-dimensional Navier–Stokes simulations are still suffering from excessive numerical dissipation, especially for vortical flow predictions, the method used here does effectively include the leading order effects that cause sinusoidal instability in a vortex pair. The two controlling factors in sinusoidal instability, i.e., the mutual and self-inductions, are intrinsically inviscid effects by all means. Therefore, it is necessary to clarify and fully understand the first-order effects, before any more complicated factors can be brought into the picture.

In the following sections, the numerical scheme used in the calculation is described in Section 2. The numerical accuracy and the advantages of the scheme are theoretically estimated. The descending speeds of two types of vortex structure are used to quantitatively validate the scheme: a single vortex ring and a vortex pair without perturbation. The computational scheme is first used in Section 3 to calculate the dispersion relation for the thin-tube vortex with a particular cut-off function employed later in the long- and short-wave perturbation computation. The development of long- and short-wave perturbations is then calculated separately. The perturbations are initially specified in displacement. The long-wave results presented in Section 4 are basically for the purpose of comparison with Crow's results for verification. In Section 5, the short-wave stable and unstable cases are simulated and discussed. Finally, the combinations of long- and short-wave perturbations are simulated in Section 6. Some nonlinear behaviour of combining two different modes is addressed. Conclusions are given in Section 7. In all the cases, only symmetric modes are considered because of the thin core structure, as explained in Reference [3].

2. NUMERICAL METHODS

2.1. Numerical schemes

The analysis begins with the three-dimensional Biot–Savart integral with a cut-off function [22]:

$$\vec{u}(\vec{x},t) = -\frac{1}{4\pi}\sum_{m=1}^{M}\Gamma_m \int \frac{(\vec{x}-\vec{x}')\times \mathrm{d}\vec{s}'}{|\vec{x}-\vec{x}'|^3} f(\vec{x}-\vec{x}') \tag{1}$$

where Γ_m is the circulation of the mth structure, M is the total number of structures in the flow field and the prime represents the dummy integral variables on each structure. The

thin-tube assumption is implied by having one filament integration on each structure. The purpose of the cut-off function is to desingularize the original Biot–Savart integration [17]. By using Rosenhead core, the cut-off function can be expressed as

$$f\left(\frac{\vec{x}}{\sigma}\right) = \frac{|\vec{x}/\sigma|^3}{(|\vec{x}/\sigma|^2+\alpha)^{3/2}} \tag{2}$$

where α is a parameter related to the fraction of circulation within the core radius $r=\sigma$. In this paper, a Gaussian core distribution is selected and the corresponding α value is 0.413 [22].

If we discretize each three-dimensional vortical curve into small segments, for Lagrangian-type motion of each node point, Equation (1) becomes

$$\vec{u}(\vec{x}_i,t) = -\frac{1}{4\pi}\sum_{m=1}^{M}\Gamma_m\sum_{j=1}^{N_m}\int_j^{j+1}\frac{(\vec{x}_i-\vec{x}')\times \mathrm{d}\vec{s}'}{(|\vec{x}_i-\vec{x}'|^2+\alpha\sigma_j^2)^{3/2}} \tag{3}$$

where N_m is the number of vortex segments on the mth vortical structure. We use a three-dimensional line for each small segment, and the line equation is

$$\frac{x'-x_j}{\Delta x_j} = \frac{y'-y_j}{\Delta y_j} = \frac{z'-z_j}{\Delta z_j}$$

where $\Delta x_j = x_{j+1}-x_j$, $\Delta y_j = y_{j+1}-y_j$ and $\Delta z_j = z_{j+1}-z_j$. Hence, if we project the integration to the x direction, we have

$$\mathrm{d}\vec{s}' = \mathrm{d}x'\left(\vec{i}+\frac{\Delta y_j}{\Delta x_j}\vec{j}+\frac{\Delta z_j}{\Delta x_j}\vec{k}\right)$$

and

$$\vec{x}_i-\vec{x}' = (x_i-x')\vec{i}+\left[(y_i-y_j)-\frac{\Delta y_j}{\Delta x_j}(x'-x_j)\right]\vec{j}+\left[(z_i-z_j)-\frac{\Delta z_j}{\Delta x_j}(x'-x_j)\right]\vec{k}$$

Therefore, the following expression can be obtained for integration with respect to the x direction:

$$\vec{u}(\vec{x}_i,t) = -\frac{1}{2\pi}\sum_{m=1}^{M}\Gamma_m\sum_{j=1,j\neq i,j+1\neq i}^{N_m}\frac{A\vec{i}+B\vec{j}+C\vec{k}}{4FD-E^2}\left[\frac{2Dx+E}{(Dx^2+Ex+F)^{1/2}}\right]_{x_j}^{x_{j+1}} \tag{4}$$

where

$$A = (y_i-y_j)\frac{\Delta z_j}{\Delta x_j}-(z_i-z_j)\frac{\Delta y_j}{\Delta x_j}$$

$$B = (z_i-z_j)-(x_i-x_j)\frac{\Delta z_j}{\Delta x_j}$$

$$C = (x_i-x_j)\frac{\Delta y_j}{\Delta x_j}-(y_i-y_j)$$

$$D = \left(\frac{\Delta y_j}{\Delta x_j}\right)^2 + \left(\frac{\Delta z_j}{\Delta x_j}\right)^2 + 1$$

$$E = -2\left[x_i + \frac{\Delta y_j}{\Delta x_j}\left(y_i - y_j + x_j\frac{\Delta y_j}{\Delta x_j}\right) + \frac{\Delta z_j}{\Delta x_j}\left(z_i - z_j + x_j\frac{\Delta z_j}{\Delta x_j}\right)\right]$$

and

$$F = \left[\left(\frac{\Delta y_j}{\Delta x_j}\right)^2 + \left(\frac{\Delta z_j}{\Delta x_j}\right)^2\right]x_j^2 + 2\left[\frac{\Delta y_j}{\Delta x_j}(y_i - y_j) + \frac{\Delta z_j}{\Delta x_j}(z_i - z_j)\right]x_j + (y_i - y_j)^2 + (z_i - z_j)^2 + x_i^2 + \alpha\sigma_j^2$$

Equations for the y and z integrations can be obtained by permutating the x, y and z variables accordingly. Notice that each straight-line element does not induce velocity on its own. Thus, when the ith point coincides with either jth or $(j+1)$th point, which are the two end points on the jth segment, the contribution from this segment is excluded. That is why in the second summation in Equation (4) we have $j \neq i$ and $j+1 \neq i$. The Adams–Bashforth second-order scheme is used for time marching, which can be expressed as

$$\vec{x}_i^{n+1} = \vec{x}_i^n + \Delta t\left[\frac{3}{2}\vec{u}^n(\vec{x}_i) - \frac{1}{2}\vec{u}^{n-1}(\vec{x}_i)\right] \tag{5}$$

where Δt is the time step. The advantage of employing exact integrations in Equation (4) will be discussed in detail in the next section.

Attention should be paid to the periodic boundary conditions used in the numerical schemes. Since the flow structure considered in this study is a pair of infinitely long vortices, end effects have to be reduced if a vortex pair with finite length is used in the simulation. Spatial periodicity in the vortex longitudinal direction has been employed in Eulerian numerical simulations for sinusoidal, Crow-type instability of the vortex pair [8–10]. Because the periodic boundary condition needs to be specified at both ends of the longitudinal direction, the Biot–Savart integration has to be carried over an infinite number of periodic images. While this can be done analytically in two dimensions [23], no such analytical expressions for the infinite summation procedure in three dimensions are known [21]. A common approach is to truncate the domain at a long enough distance where the end effects on the centre portion of the domain become minimal and only the centre portion is selected for analysis. However, in one of our early test cases for a problem involving a vortex pair, such an approach has resulted in a structure shown in Figure 1, where the tails at the two ends are amplified when the time marching proceeds. Therefore, the nearest-neighbour-image concept, introduced by Ashurst and Meiburg [20], is implemented. The concept can be illustrated by Figure 2, where different images of the segments are taken into account. For example, the vortex filament

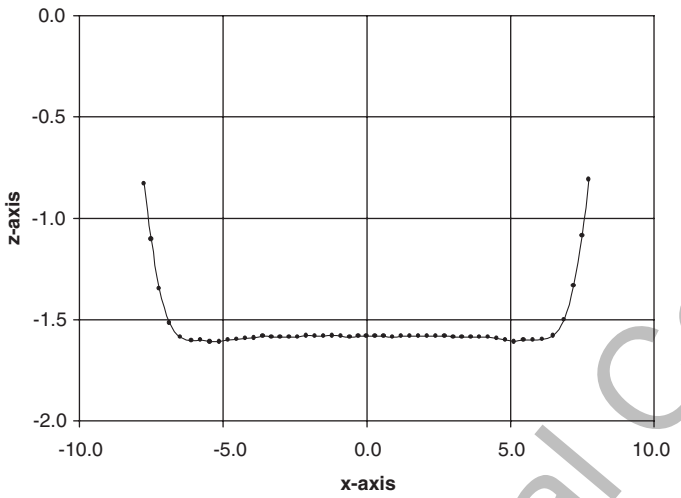

Figure 1. End effects due to the downward motion of the vortex pair.

segment at x_{j0} and its periodic image at x_{j1}, which is closer to x_i than the other periodic image at x_{j2}, are taken for evaluating the velocity at point x_i and the image at x_{j2} is not taken. On the other hand, when the velocity at x_k is evaluated, x_{j0} and its image at x_{j2}, which now is closer to x_k than x_{j1}, are used.

2.2. Accuracy analysis

A noticeable advantage of using the exact integration can be seen, instead of using a summation of

$$\vec{u}(\vec{x}, t) = -\frac{1}{4\pi}\sum_{m=1}^{M}\sum_{j=1}^{N_m}\Gamma_m \frac{(\vec{x}^c_{m,j} - \vec{x}) \times (\vec{x}_{m,j+1} - \vec{x}_{m,j})}{|\vec{x}^c_{m,j} - \vec{x}|^3} f\left(\frac{|\vec{x}^c_{m,j} - \vec{x}|}{\sigma}\right) \tag{6}$$

where

$$\vec{x}^c_{m,j} = \frac{1}{2}(\vec{x}_{m,j} + \vec{x}_{m,j+1})$$

The accuracy of using the expression in the second summation in Equation (6) is $O(|\vec{x}_{m,j+1} - \vec{x}_{m,j}|^2)$. Therefore, when the vortex stretching occurs, the accuracy becomes worse and additional points need to be added in the stretched segment. A usual practice is every time when $|\vec{x}_{m,j+1} - \vec{x}_{m,j}|$ is two times of its initial value, the segment is split into two segments. In the current calculation, if the vortex stretching happens, the relative curvature is reduced which can compensate for the errors due to longer segment lengths, thus no points need to be added to reduce the errors. On the other hand, when vortex shrinking occurs, the number of points automatically increases in the shrinking region to reduce the errors caused by curvature effects due to the straight-line approximation for the vortex segment.

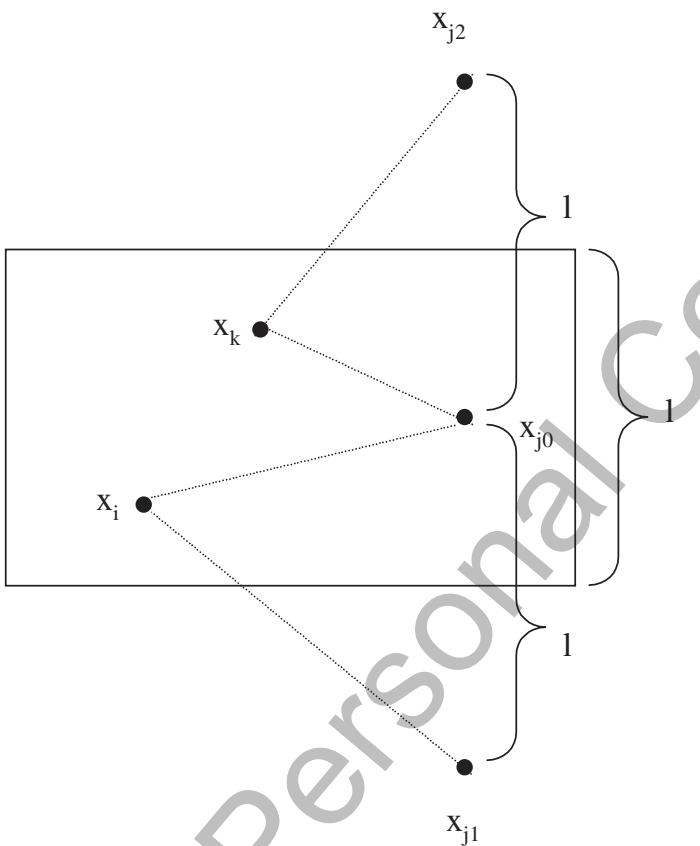

Figure 2. Illustration of the nearest-neighbour-image method by Ashurst and Meiburg [20], where l is the simulation domain size.

In order to mathematically explain the above argument, we look at the integration in one segment, as shown in Figure 3. Without losing generality of the argument, we can treat the problem in two dimensions, and define a functional as

$$I = \int_{-\Delta x/2}^{\Delta x/2} L(x, y)\,\mathrm{d}x \tag{7}$$

where

$$y = y(x)$$

is the integral path function of the integrand L. If the scheme as in Equation (6) is used, the functional becomes

$$I_1 = \int_{-\Delta x/2}^{\Delta x/2} L(0, y(0))\,\mathrm{d}x = L(0, y_o)\Delta x \tag{8}$$

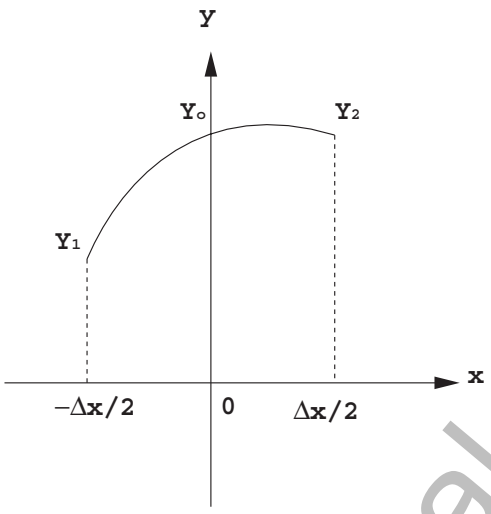

Figure 3. Illustration of one integral segment.

If exact integration is performed on each line segment of the vortex filament, we have

$$
\begin{aligned}
I_2 &= \int_{-\Delta x/2}^{\Delta x/2} L\left(x, \frac{y_2 - y_1}{\Delta x}\, x + \frac{y_2 + y_1}{2}\right) \mathrm{d}x \\
&= L\left(0, \frac{y_1 + y_2}{2}\right) \Delta x + \int_{-\Delta x/2}^{\Delta x/2} \sum_{1}^{\infty} \frac{1}{n!} \left(x \frac{\partial}{\partial x} + \frac{y_2 - y_1}{\Delta x}\, x \frac{\partial}{\partial y}\right)^n L\left(0, \frac{y_1 + y_2}{2}\right) \mathrm{d}x \\
&= L\left(0, \frac{y_1 + y_2}{2}\right) \Delta x + \sum_{1}^{\infty} \frac{(\Delta x)^{2n+1}}{2^{2n}(2n+1)!} \left(\frac{\partial}{\partial x} + \frac{y_2 - y_1}{\Delta x}\, \frac{\partial}{\partial y}\right)^{2n} L\left(0, \frac{y_1 + y_2}{2}\right) \qquad (9)
\end{aligned}
$$

where $\partial/\partial x$ and $\partial/\partial y$ mean to take derivatives for the first and second variables in $L(x, y)$, respectively. We further expand y_1 and y_2 at $x = 0$, and I_2 becomes

$$
\begin{aligned}
I_2 &= L(0, y_o)\Delta x \\
&\quad + (\Delta x)^3 \left[\frac{L_y(0, y_o)}{4}\, y''(0) + \frac{L_{xx}(0, y_o)}{24} + \frac{L_{xy}(0, y_o)}{12}\, y'(0) + \frac{L_{yy}(0, y_o)}{24}\, (y'(0))^2\right] \\
&\quad + O((\Delta x)^5) \qquad (10)
\end{aligned}
$$

In order to determine the accuracy of integration using I_1 or I_2, we use a second-order polynomial curve to approximate the integral path. We then have

$$
I_3 = \int_{-\Delta x/2}^{\Delta x/2} L\left(x, y(0) + x y'(0) + \frac{x^2}{2}\, y''(0)\right) \mathrm{d}x
$$

$$= L(0, y_o)\Delta x + \int_{-\Delta x/2}^{\Delta x/2} \sum_{1}^{\infty} \frac{1}{n!} \left\{ x \frac{\partial}{\partial x} + \left[xy'(0) + \frac{x^2}{2} y''(0) \right] \frac{\partial}{\partial y} \right\}^n L(0, y_o)\, \mathrm{d}x$$

$$= L(0, y_o)\Delta x + (\Delta x)^3 \left[\frac{L_y(0, y_o)}{24} y''(0) + \frac{L_{xx}(0, y_o)}{24} + \frac{L_{xy}(0, y_o)}{12} y'(0) + \frac{L_{yy}(0, y_o)}{24} (y'(0))^2 \right] + O((\Delta x)^5) \tag{11}$$

In comparison of Equations (8) and (11), and Equations (10) and (11), it can be seen that the integrations of both I_1 and I_2 have an accuracy of $O((\Delta x)^3)$. However,

$$|I_3 - I_1| = (\Delta x)^3 \left| \frac{L_y(0, y_o)}{24} y''(0) + \frac{L_{xx}(0, y_o)}{24} + \frac{L_{xy}(0, y_o)}{12} y'(0) + \frac{L_{yy}(0, y_o)}{24} (y'(0))^2 \right| + O((\Delta x)^5)$$

while

$$|I_3 - I_2| = (\Delta x)^3 \left| \frac{5L_y(0, y_o)}{24} y''(0) \right| + O((\Delta x)^5)$$

Therefore, the difference in the two truncation errors is that the leading-order truncation error in I_2 is only influenced by $y''(0)$, which represents the curvature of the curve. If this error is controlled at the initial time, then once there is stretching, the curvature becomes smaller, thus curbs the growth of errors. If there is shrinking, then Δx becomes smaller. Although $y''(0)$ may increase during shrinking, the net errors can remain small. On the other hand, the error in I_1 also includes $y'(0)$, which is not controlled by the algorithm, therefore Δx has to remain all time small, and adding points is required to split Δx once Δx is significantly prolonged. If the error of each term in a summation for integration is $O((\Delta x)^3)$, the error of the integration itself is $O((\Delta x)^2)$, as in Equations (4) and (6).

2.3. *Validation cases*

Two test cases have been selected for validating the numerical scheme. The first one is a thin vortex ring. This case has been historically used for validating vortex core smooth functions in the cut-off method and the resolution convergence requirement for the length of each element of the ring filament. The constant translational speed of the ring can be expressed as, in the absence of viscosity [24],

$$V = \frac{\Gamma}{4\pi R} \left[\log\left(\frac{8R}{\sigma} \right) + C \right] \tag{12}$$

where Γ is the circulation, the inner radius σ is small in comparison with the outer radius R, and the constant C depends on the distribution of vorticity within the ring. For the Gaussian vorticity distribution, the value of C is -0.558. Non-dimensionalization was performed based on Γ and R. The test case was run with the core radius equal to the ring inner radius, $\sigma = 0.1$.

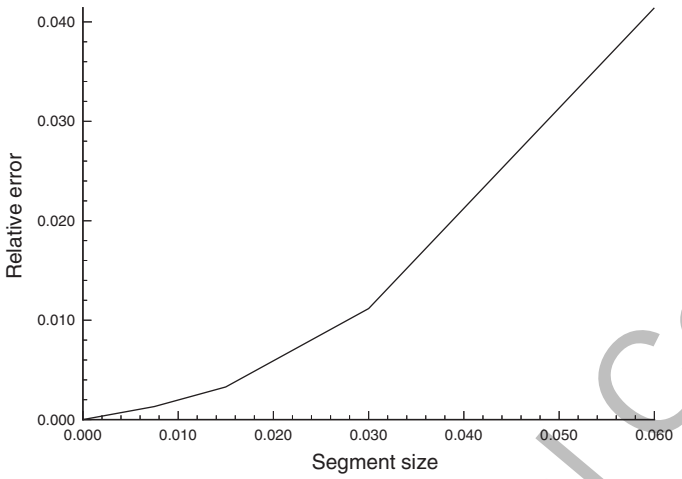

Figure 4. Relative error of the descending speed of the vortex pair versus the vortex segment length.

With this core size, the analytical value of the descending speed calculated from Equation (12) is 0.3043. The computed descending speed values with segment lengths of 0.06, 0.03, 0.015 and 0.0075 are 0.2917, 0.3009, 0.3033 and 0.3039, respectively. Figure 4 graphically shows the trend of the relative error change versus the segment length size. The errors can be as low as $O(10^{-3})$, when the segment length is smaller than 0.015 which is less than half of the ring inner radius. This indicates that overlapping between neighbouring vortex elements is necessary when there is curvature in the vortex filament.

The second test case is an infinitely long, straight-line vortex pair which translates due to mutual induction. This case is used to verify the performance of the nearest-neighbour-image method implemented in the numerical scheme and to determine the necessary number of images required for the simulation. The result shows that at any instant, the vortex structure remains straight lines. That means the method does not distort the vortex structure. The translational speed of an infinitely long vortex pair with cut-off function has an analytical solution:

$$V = \frac{\Gamma}{2\pi b} f\left(\frac{b}{\sigma}\right) \tag{13}$$

where Γ is the circulation of the vortex and b is the vortex pair spacing. For a Gaussian core of radius 0.1, the dimensionless speed based on Γ and b is 0.1582. Test cases with filament lengths of 8, 16, 24 result in translational speed of 0.1537, 0.1573 and 0.1580. Therefore, it has been concluded that for the nearest-neighbour-image method to achieve accuracy of $O(10^{-3})$ for the translational speed of the vortex pair, a minimum length of 24 vortex spacing is necessary. The reason is that the influence of the vortex filament of longer than that length (plus its image lengths) can be neglected, although the influence is the sum of all the truncated length. It should be noted that such a conclusion is only for the vortex pair structure, which is the structure of the current problem. Other structures may result in different length requirement for the nearest-neighbour-image method simulation. In Reference [20], three images at each end of the periodic boundary condition was suggested without giving detailed reasoning. It

is also noted that in this test case, the size of each segment does not have influence on the results simply because of the following three reasons: the translational speed is only caused by mutual induction; the vortex structure is a straight line; and the exact integration, Equation (4), along each segment line is calculated.

This is a non-trivial test case. Although the absolute translational speed does not influence the stability behaviour of the vortex system, which is the zeroth order effect of the mutual induction, the first order effect (due to the mutual induction from perturbed displacement of one vortex to the other) cannot be estimated at this point and in order not to truncate the first order effects, the zeroth order effect is used as an indication to investigate the influence of the truncation of images.

3. DISPERSION RELATIONS

The computational method was first used to calculate a dispersion relation for a thin tube vortex with the cut-off function expressed in Equation (2). It was pointed out in Reference [2] that in Crow's analysis [1], the short-wave modes are spurious, due to the long-wave assumptions used in the analysis. The dispersion relation in Crow's paper is the same as the one by Kelvin [25] and is based on the asymptotic expansion of the solution for a ring which can be expressed as

$$\Omega = -\frac{(k\sigma)^2}{4\pi}\left[\ln\frac{1}{k\sigma} + \frac{1}{4} + \ln 2 - \gamma\right] \tag{14}$$

where Ω is the normalized (by Γ/σ^2) rotating frequency of the sinusoidal disturbance due to self-induction, γ is Euler constant with a value of 0.5772, and k is the axial wave number. Around the zero self-induction frequency is the region where the unstable sinusoidal wave can possibly develop. Obviously, the first zero (at $k\sigma = 0$) is where the long-wave instability occurs. The second zero point is at $k\sigma = 1.44$, according to Equation (14). This point is claimed to be spurious, since it only happens when the asymptotic expansion for long-wave ($k\sigma \ll 1$) is performed to obtain Equation (14). There is a dispersion relation in Moore and Saffman [26] (which was originally from Krishnamoorthy [27]), when without axial flow

$$\frac{g^2}{4\Omega_0^2 - g^2}\left[\beta\sigma\frac{J'_{|p|}(\beta\sigma)}{J_{|p|}(\beta\sigma)} + \frac{2p\Omega_0}{g}\right] = -\sigma|k|\frac{K'_{|p|}(|k|\sigma)}{K_{|p|}(|k|\sigma)} \tag{15}$$

where

$$g = -\Omega + p\Omega_0$$

$$\beta^2 = k^2(4\Omega_0^2 - g^2)/g^2$$

p is the azimuthal wave number, Ω_0 is the vorticity of solid-body rotation of the undisturbed vortex, and $J_{|p|}$ is the $|p|$th order Bessel function of the first kind and $K_{|p|}$ is the $|p|$th order modified Bessel function of the second kind. Widnall *et al.* [2] showed that for the bending mode (when $|p| = 1$, which is the mode related with sinusoidal perturbation) Ω monotonically increases with $k\sigma$ starting with $\Omega = 0$ and $k\sigma = 0$ (the zeroth radial mode).

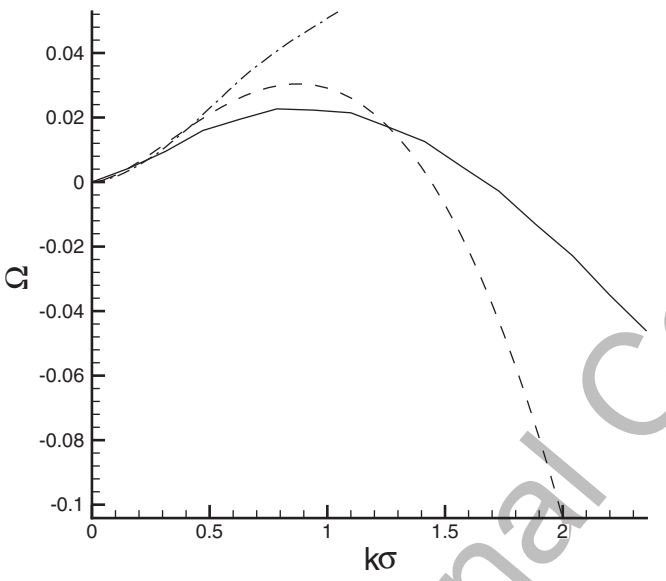

Figure 5. Dispersion relations. The solid line is for the computed results using the thin-tube vortex method, the dash line is the result from Equation (14), and the dash-dot line is the result from Equation (15).

Therefore the second zero can never be reached. However, from Wang's [18, 28] thin-tube vortex simulations, a second zero frequency around $k\sigma = O(1)$ occurs for thin-tube vortices. Although the shape and location of the second zero change with cut-off functions used in the simulations, all the shapes are similar and the locations of the second zeroes are close to $k\sigma = O(1)$. The cut-off functions tested in Reference [18] are

$$\begin{aligned} f(r) &= \begin{cases} 1, & r > 1 \\ r^3, & r \leqslant 1 \end{cases} \\ f(r) &= \tanh(r^3) \\ f(r) &= 1 + \left(\frac{3}{2} r^3 - 1\right) \exp(-r^3) \\ f(r) &= \tanh(r^3) + \frac{3}{2} r^3 \frac{1}{\cosh^2(r^3)} \end{aligned} \tag{16}$$

In Wang's results, the zero rotating frequency near $k\sigma = O(1)$ is at $k\sigma$ value between 1.5 and 2.5 for all the tested cut-off functions listed in Equation (16).

The dispersion relation for using the cut-off function in Equation (2) is numerically calculated and the result is plotted in Figure 5, along with the result from the long-wave asymptotic expansion, Equation (14), and Moore and Saffman's [26] result, Equation (15). It should be noted that in the thin-tube vortex simulation, the long-wave assumption is not enforced. The only assumption is the thin-tube assumption, that is, the vortex core does not change its size and structure during the simulations. It shows that a second zero of the rotating frequency is

at $k\sigma = 1.72$, not too far away from the asymptotic expansion result. It needs to be pointed out that Equation (15) is valid under the assumption that the core vorticity is constant, while in the thin-tube vortex method the core vorticity changes due to the stretching and shrinking of the vortex segment. Therefore, it can only be speculated that the difference in the dispersion relations between thin-tube vortex method and Equation (15) is due to the different assumptions made in each model. In Reference [12], a short-wave instability was measured near $k\sigma = 1.6$. That instability, however, attributed to the vortex core deformation in Reference [12] which was related to a $p = 1$ bending wave mode instead of a $p = 0$ mode. The flow physics related to these phenomena has not yet been fully determined. In the following two sections, the long and short-wave sinusoidal perturbations are simulated to investigate the influence from the dispersion relation.

4. LONG-WAVE SINUSOIDAL PERTURBATIONS

The thin-tube vortex method developed in Section 2 is now used to simulate the vortex pair undergoing sinusoidal perturbations. A pair of counter-rotating, straight line vortices is initially perturbed with a sinusoidal displacement. All the simulations are non-dimensionalized using the vortex pair circulation, Γ, and the undisturbed spacing, b. The x direction is in the axial direction of the vortex and the y and z directions are the span and vertical directions, respectively. The initial position of the vortex pair in the coordinate system is shown in Figure 6. The initial disturbances are specified as sinusoidal displacement in both the

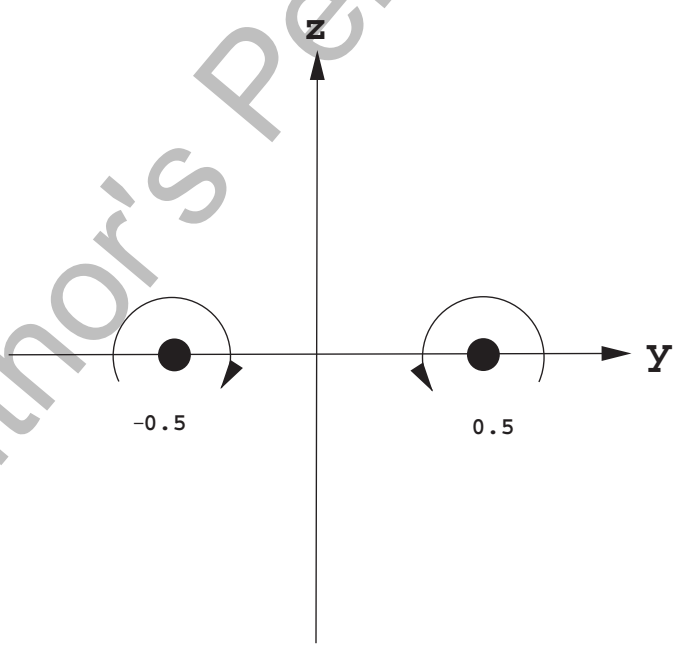

Figure 6. The initial position of the vortex pair and the coordinate system used in the simulations.

y and z directions,

$$D = a_m \sin(kx) \tag{17}$$

where a_m is the disturbance amplitude and k is the wave number. Since the y and z directions are specified with the same disturbances, the initial planar standing-wave angle, defined as $\theta = \tan^{-1}(a_{mz}/a_{my})$, is 45°. Only the symmetric mode is simulated. Since the symmetry is with respect to the $y = 0$ plane, only the vortex in the $y > 0$ domain needs to be simulated and the symmetry image is added for the effects from the vortex in the $y < 0$ part.

For the first case, a vortex pair with core radius of 0.1 is initially perturbed with a wave number of $k = 0.75$ and a displacement of $a_m = 0.05$ as defined in Equation (17). The wave number is corresponding to a wavelength of 8.38. The simulating filament length is selected as 8π, according to the vortex pair test case in the previous section which requires more than 24 vortex pair spacing. That includes three periodic waves in the simulation for the purpose of checking periodicity. A total of 500 elements are initially distributed on the filament uniformly to satisfy the resolution requirement with the segment length less than half of the core radius. The initial position of the simulated vortex is at $y = 0.5$ and $z = 0$, with the vortex axis spanning from $x = -4\pi$ to $x = 4\pi$. A time step size of 0.005 was used in the second-order Adams–Bashforth time marching.

Figure 7 shows the time histories of the disturbance development for this case in the x–y and x–z planes. The wave is actually stationary, since the rotating frequency is almost zero in long-wave regimes, according to the dispersion relation in Figure 5. The disturbances in the y and z directions are always in phase. The standing wave angle starts at 45°. Because of the uneven induction from the other vortex, which produces slightly stronger downward motion on the portion of the wave close to each other, the planar standing-wave angle becomes about 60° at the end of the simulation ($t = 14$).

It can be seen that towards the end of the simulation, the curvatures of the wave at the closest part of the two vortices are increased, while those at the farthest are decreased. Such a nonlinear effect has also been shown in the nonlinear analysis of Klein and Majda [14]. The simulation was terminated at dimensionless time of 14, when the $y_{\min}$ in the waves almost reaches 0.1, the vortex core radius. That means the closest points of the two vortices in the vortex pair almost touch. After that, peculiar shapes of the waves occur, which obviously are non-physical.

The amplitude grows with time exponentially. The amplitude versus time is plotted in Figure 8. To compare with Crow's prediction, the following definition of the amplification rate is utilized:

$$\ln \frac{a_m(t)}{a_m(0)} = a^* t \tag{18}$$

where a^* is the amplification rate. The instantaneous amplitude, $a_m(t)$, is defined as

$$a_m(t) = \frac{1}{2}\sqrt{[y_{\max}(t) - y_{\min}(t)]^2 + [z_{\max}(t) - z_{\min}(t)]^2} \tag{19}$$

In Reference [1], the amplification rate for the symmetric modes has been derived as

$$a^* = \frac{1}{2\pi}[(1 - \psi(k) + k^2\omega)(1 + \chi(k) - k^2\omega)]^{1/2} \tag{20}$$

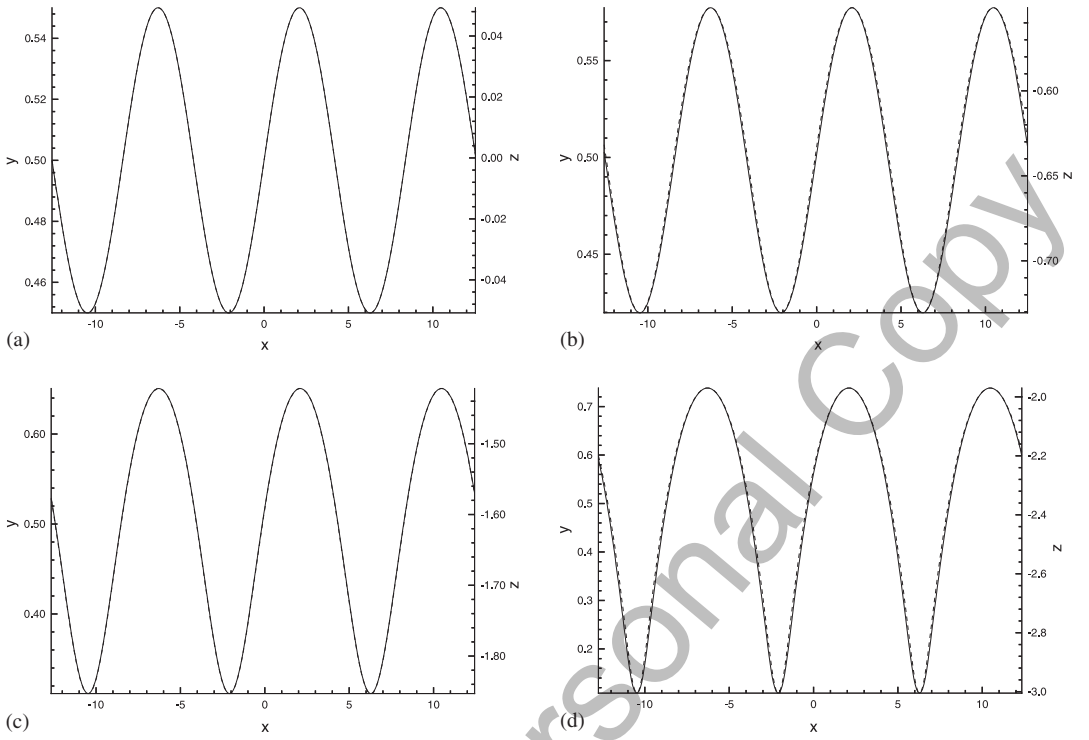

Figure 7. Long-wave perturbation development histories for the case of $k = 0.75$ and $\sigma = 0.1$. The solid curve is for the y-direction component and the dashed curve is for the z-direction component. (a) $t = 0$, (b) $t = 4$, (c) $t = 10$, (d) $t = 14$.

where $\psi(k) = k^2 K_0(k) + kK_1(k)$, $\chi(k) = kK_1(k)$, and K_0 and K_1 are modified Bessel functions of the second kind, and ω is defined as

$$\omega(\delta) = \frac{1}{2}\left[(\cos\delta - 1)/\delta^2 + \sin\delta/\delta - Ci(\delta)\right] \tag{21}$$

where $\delta = 0.642\sigma$ and $Ci(\delta)$ is the cosine integral, according to Crow [1]. It can be seen in Figure 8 that the amplification rate of the computational results are in good agreement with Crow's prediction, until after long-time interactions when the troughs of the waves are close to each other and nonlinear effects start to show, as also shown in Figure 7. The amplification rate is increased towards the end of the simulation due to enhanced mutual induction.

The second case is the same as the first one, except that the vortex core radius is 0.25, to investigate the core size effects. The growth rate is plotted in Figure 8 along with the core radius of 0.1 case for comparison. Figure 9 is the time histories of the wave in the x–y and x–z planes. It can be seen that the growth rate is lower, therefore the simulation can run longer and even at the point when the two vortices touch, the simulation can still continue, contrary to the 0.1 core radius case where the simulation has to be stopped. This is due to the fact that the larger core provides a smoothing mechanism that reduces the curvature when the two vortices are getting closer, which can be seen by comparing Figures 9 and 7.

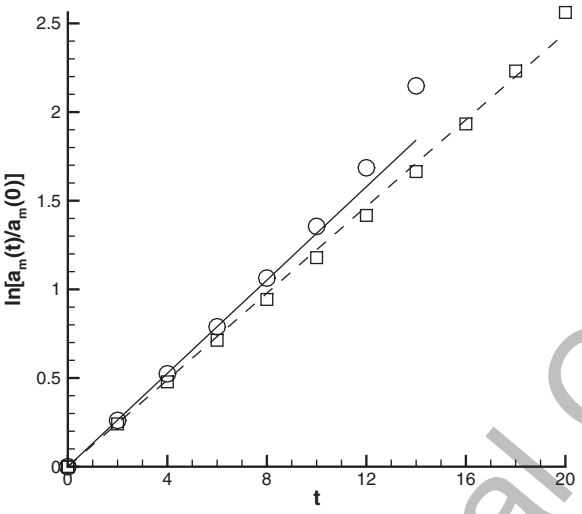

Figure 8. Long-wave perturbation amplitude growth histories. The solid line is for the case of $k = 0.75$ and $\sigma = 0.1$ using Equation (20) and the circle symbols are the computed results for the same case. The dash line is for the case of $k = 0.75$ and $\sigma = 0.25$ using Equation (20) and the square symbols are the computed results for the same case.

Towards the end of the simulation, the planar standing-wave angle is also close to 60°. This means in unstable cases, the standing wave angles are controlled by mutual inductions and are independent of the core size.

5. SHORT-WAVE SINUSOIDAL PERTURBATIONS

The simulation conditions for the short-wave cases are the same as those of long-wave cases, except the wave number, k, is 7, which is corresponding to a wavelength of 0.898. The same two core radius sizes in the long-wave cases are considered, that is, 0.1 and 0.25. Figures 10 and 11 show the time histories of the disturbance development for the two short-wave cases in the x–y and x–z planes. For the purpose of clarity of the graphs, only a section of waves in $-5 \leqslant x \leqslant 5$ is plotted, although the simulation domain is still $-4\pi \leqslant x \leqslant 4\pi$.

Figure 10(a) is the initial vortical curve shape and it shows that the sinusoidal disturbances in the y direction is in phase of the disturbances in the z direction. When it reaches $t = 4$ (Figure 10(b)), the amplitude in the y direction grows about 50 per cent, from 0.05 to 0.075, while the amplitude in the z direction reduces to 0.014, resulting in a planar standing-wave angle of 11°. The disturbances are still in phase between the two directions. At $t = 10$, the disturbances in the two directions are out of phase. The amplitude in the y direction is about 0.056, and the amplitude in the z direction is 0.042, which gives a planar standing-wave angle of $-36°$. At $t = 14$, the disturbances are still out of phase. The amplitude in the y direction is reduced back to about 0.017, while the amplitude in the z direction grows to 0.062. The planar standing-wave angle is then $-75°$. At $t = 18$, the amplitude of the y-direction disturbance becomes 0.027, and the z-direction amplitude is about 0.14. The two disturbances

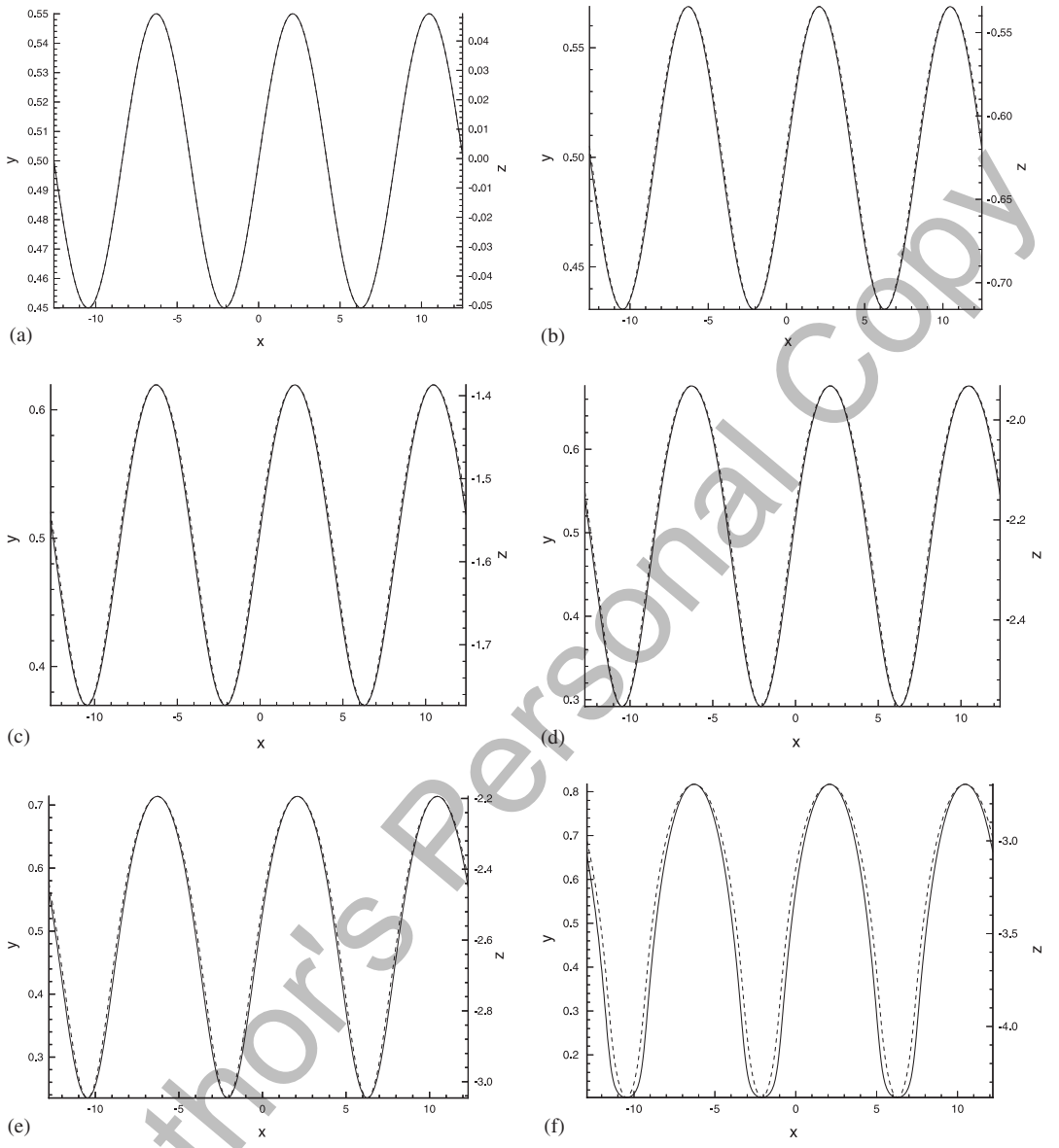

Figure 9. Long-wave perturbation development histories for the case of $k = 0.75$ and $\sigma = 0.25$. The solid curve is for the y-direction component and the dashed curve is for the z-direction component. (a) $t = 0$, (b) $t = 4$, (c) $t = 10$, (d) $t = 14$, (e) $t = 16$, (f) $t = 20$.

are in phase. The planar standing-wave angle is now 80°, or more precisely, −100°, since the y-direction disturbance is switched 180°. The disturbances keep in phase at $t = 20$, with the amplitudes in the y and z directions approximately equal to 0.046 and 0.052, respectively, therefore the planar standing-wave angle is 50°, or −130°. The time change of the planar

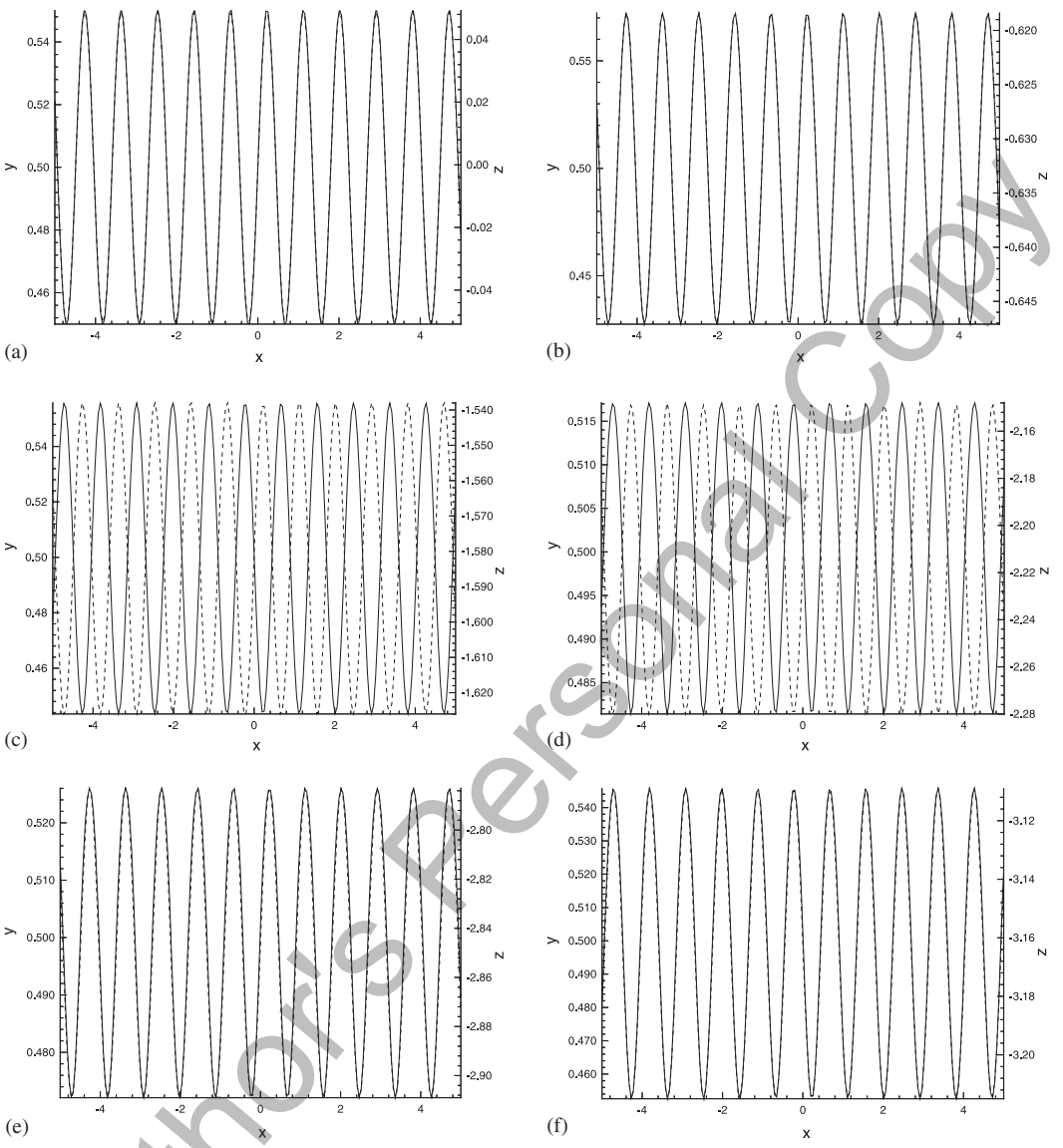

Figure 10. Short-wave perturbation development histories for the case of $k = 7$ and $\sigma = 0.1$. The solid curve is for the y-direction component and the dashed curve is for the z-direction component. (a) $t = 0$, (b) $t = 4$, (c) $t = 10$, (d) $t = 14$, (e) $t = 18$, (f) $t = 20$.

standing-wave angle, θ, versus time is plotted in Figure 12. It can be seen that the average angular speed of the disturbance rotation is about 8.6° per unit time. The rotational direction is clockwise, which is in the opposite direction of the vortex circulation. It should be noted that in unstable cases, the planar standing-wave angle asymptotes to a certain value and the wave does not rotate.

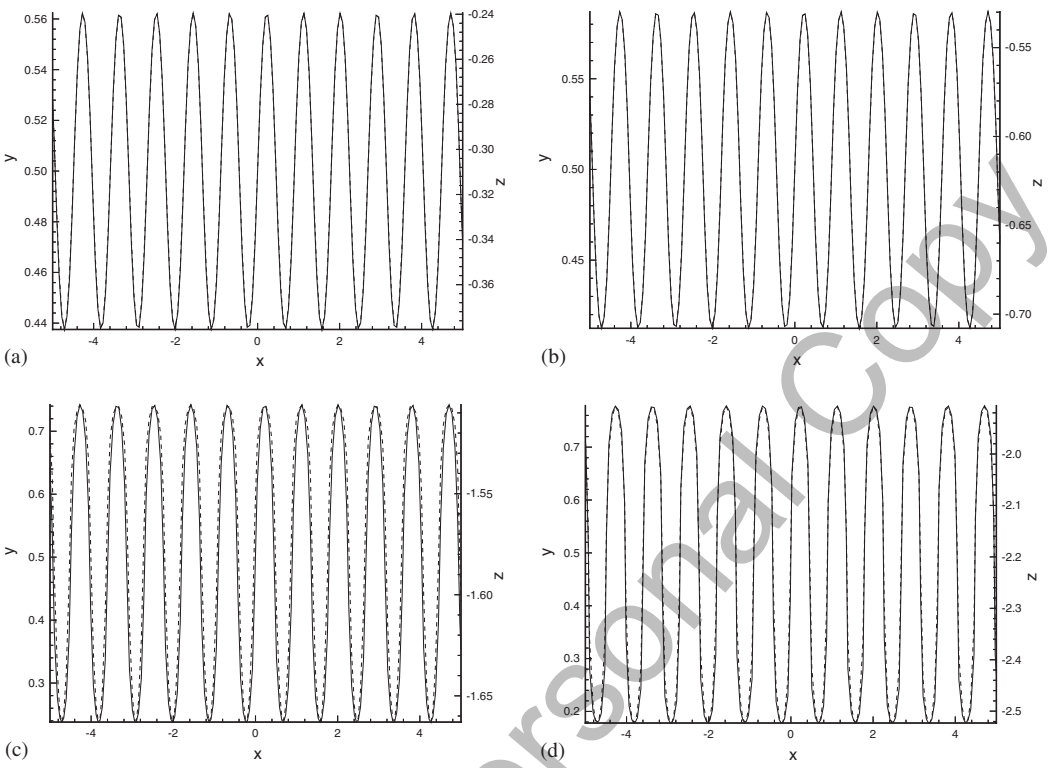

Figure 11. Short-wave perturbation development histories for the case of $k = 7$ and $\sigma = 0.25$. The solid curve is for the y-direction component and the dashed curve is for the z-direction component. (a) $t = 2$, (b) $t = 4$, (c) $t = 10$, (d) $t = 14$.

The behaviour in Figures 10(a)–(f) shows that the vortex pair is neutrally stable, since there is no mechanism to dampen the disturbances. The disturbances rotate in the opposite sense to the rotation of the vortex. The self-induction is dominant over the mutual induction caused by the other vortex. The only significant effect from the mutual induction is the descent of the vortex pair. The descending speed is 1.56, approximately equal to the descending speed of an unperturbed vortex pair. Those results are in agreement with Crow's linear analysis.

Figure 11 is a case for unstable short-wave perturbations. The size of core radius is 0.25, resulting in $k\sigma = 1.75$, which is close to the zero self rotation according to the dispersion relation in Figure 5. Therefore, it is a short-wave unstable case. In Figure 11, the y- and z-direction components of the waves are in phase all the time. The planar standing-wave angle remains approximately 45°, contrary to the long-wave unstable cases where the planar standing-wave angle becomes close to 60°. Because of the growth of the wave amplitude, the simulation was terminated at $t = 14$, since peculiar wave shapes emerge due to the overlapping of the vortex with its symmetry image after this time level. The amplitude growth history was calculated using the same definition in Equation (19) and is plotted in Figure 13. At this wave length and core size, Crow's analytical result, Equation (20), does not apply since the

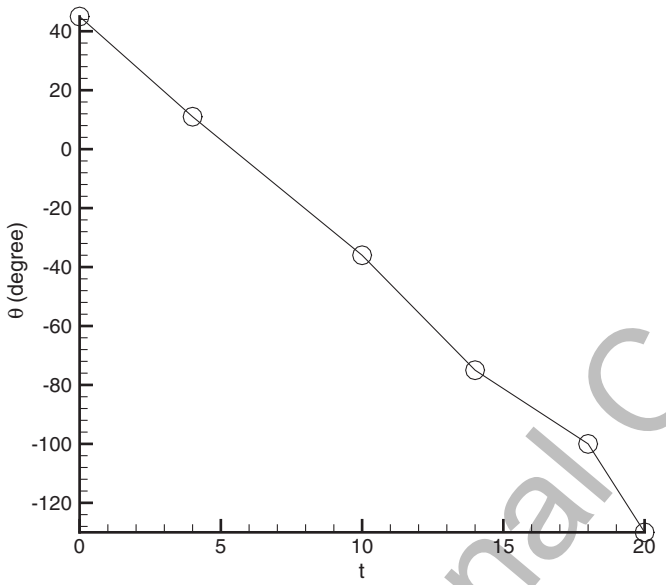

Figure 12. Planar standing-wave angle versus time for the short-wave stable case.

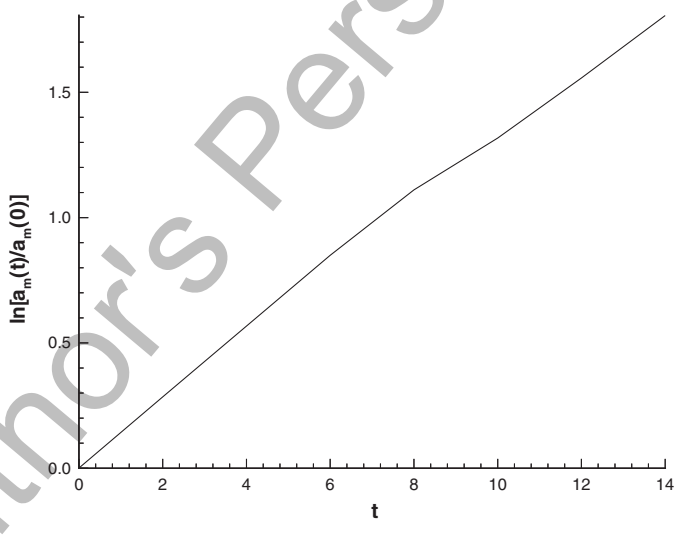

Figure 13. Computed short-wave perturbation amplitude growth history for the case of $k = 7$ and $\sigma = 0.25$.

amplification rate calculated from that equation is imaginary. Therefore, there is no counterpart of Crow's results plotted. It can be seen that the growth rate is almost as high as the long-wave cases, in comparison with Figure 8.

6. COMBINED LONG- AND SHORT-WAVE PERTURBATIONS

The long-wave ($k_1 = 0.75$) and short-wave ($k_2 = 7$) perturbations in Sections 4 and 5 are combined to study the effects when both wave numbers appear at the same time in the perturbations. The two core sizes (0.1 and 0.25) are also selected, at which the long-wave cases are unstable. For the short waves, one is stable ($\sigma = 0.1$) and the other is unstable ($\sigma = 0.25$). The simulation conditions are the same as in Sections 4 and 5, with the initial perturbations specified as

$$D = a_{m1} \sin(k_1 x) + a_{m2} \sin(k_2 x) \tag{22}$$

where the amplitudes of each wave, a_{m1} and a_{m2}, are chosen as 0.05 and 0.005, respectively.

The perturbation development histories for the case of $\sigma = 0.1$ are shown in Figure 14. It can be seen that the instability of the long-wave perturbations does not change the stability behaviour of the short-wave part, and vice versa (by comparing Figures 14 and 7). However, in the case when both the long- and short-wave perturbations are unstable, which is shown in Figure 15, the growth rate of the peak is much higher, in comparison with Figure 9, in the portion of the wave that is close to the image vortex (the image vortex is at the other side of $y = 0$). The short-wave portion that is far away from the image vortex has much weaker mutual

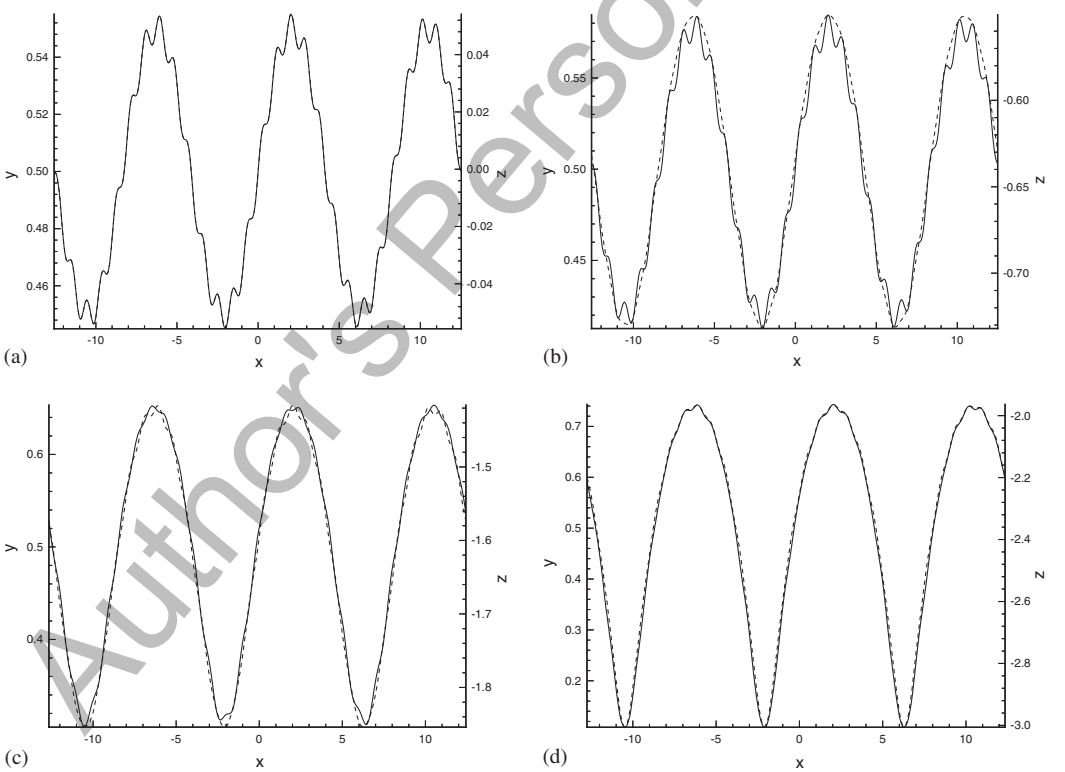

Figure 14. Perturbation development histories for combined long- and short-wave perturbations for the case of $k_1 = 0.75$, $k_2 = 7$ and $\sigma = 0.1$. (a) $t = 0$, (b) $t = 4$, (c) $t = 10$, (d) $t = 14$.

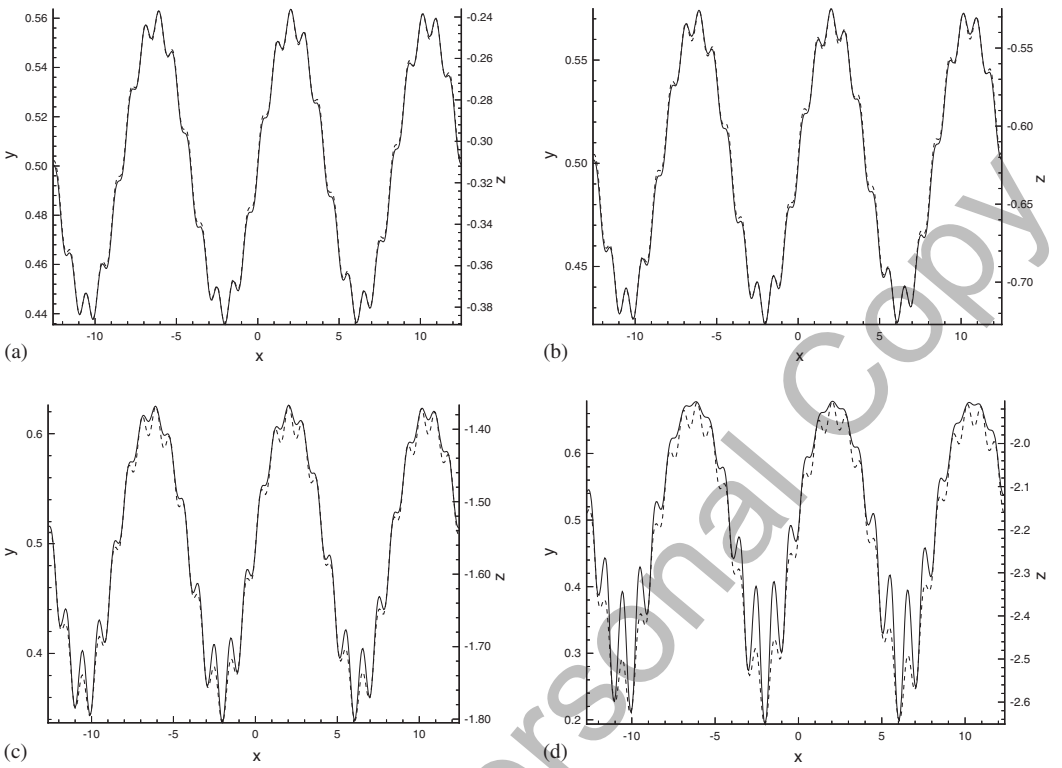

Figure 15. Perturbation development histories for combined long- and short-wave perturbations for the case of $k_1 = 0.75$, $k_2 = 7$ and $\sigma = 0.25$. (a) $t = 2$, (b) $t = 4$, (c) $t = 10$, (d) $t = 14$.

induction than the portion near it. Therefore, the amplification rate is enhanced by the long-wave instability which causes much closer separation at those locations. On the other hand, the long-wave instability causes some portion of the short waves farther away from the influence of the image vortex and that portion shows very little growth of short-wave instability. That means that the instability, which is caused by the mutual induction of the two vortices in the vortex pair, can be amplified or reduced at different axial locations by superimposing another unstable mode perturbations. These effects are obviously non-linear which are due to the interaction between the two modes, in addition to the non-linear effects of each mode itself by having asymmetric wave amplification (with respect to the initial mean position of the vortex at $y = 0.5$). The experiment by Leweke and Williamson [12] also showed larger short-wave amplification in the portion of the waves in which the stronger mutual induction is due to the closeness of the two vortices caused by the long-wave instability. They explained the mechanism of such combined instability using elliptic streamline theory.

The enhancement and weakening of unstable short waves by unstable long waves may seem to be intuitive, in the sense that the closeness of the two vortices increases the mutual induction thus enhances the instability, and the separation of the two vortices reduces the amplification of the instability. However, the fact that the long-wave instability has no influence on the superimposed stable short waves is perplexing. It is noticed that the vortex core size is

characterized by the separation of the two vortices. Therefore, when the separation distance is reduced 2.5 times, the relative core size is increased 2.5 times. That is, if the original core size is $\sigma = 0.1$ at the separation of $b = 1$, which is the stable short-wave case here at the initial condition, then when the long waves grow to a point where some portion of the separation of the two vortices is 0.4, the relative core size becomes 2.5, which is in the short-wave unstable regime. Yet the instability of short waves does not occur, according to Figure 14. One could argue that the portion of close separation (which is about 0.4 of the initial span of the vortex pair) was only several short-wave-lengths long. The Crow instability requires mutual induction from theoretically infinitely long vortices. Therefore the short-wave instability would not show. Based on that argument, we can only deduce that although the closeness of the two vortices due to instability of long-wave perturbations can create a local environment for short-wave instability, the latter does not occur in the simulation, because of the limited mutual induction from the relatively short lengths of the close part of the other vortex.

7. CONCLUSIONS

The vortex method developed here has made use of analytical integrations to reduce the errors caused by vortex segment stretching and shrinking. End effects have been successfully reduced by using the nearest-neighbour-image method. In the selected validation cases, the descending speeds are accurately matched for a vortex ring and a pair of straight-line, counter-rotating vortices. The unstable, long-wave perturbation growth rates agree quantitatively with Crow's analysis until towards the end of the simulations when the two vortices are close, causing slightly faster growth rates. The planar standing-wave angle becomes 60° after initial time marching. It is controlled by mutual inductions and is independent of the vortex core size. Simulation results of the vortex pair perturbed by short-wave perturbations have shown that for a stable case, the vortex pair is neutrally stable and the disturbances rotate around each vortex centreline in the opposite sense of the vortex circulation, which is in agreement with Crow's theory. A zero self-rotation frequency at $k\sigma = 1.72$ has been found in zeroth radial mode for bending in the dispersion relation simulation for a single vortex with the cut-off function used in this paper. A short-wave perturbation case has then been simulated near the zero self-rotation and instability has been detected. The growth rate is comparable with its long-wave counter-part, however, with a planar standing-wave angle of 45°. The combined long- and short-wave perturbation cases have shown that if the long-wave mode is unstable but the short-wave mode is stable, no significant coupling effects occur. However, when both the modes are unstable, a non-linear effect occurs. The growth rate of the peak is much higher, in comparison with the single long-wave mode case, in the portions of the waves that are close to the image vortex at the other side of the symmetry axis.

ACKNOWLEDGEMENTS

The author would like to gratefully acknowledge Dr H. Wang at University of California Santa Cruz, for providing his Ph.D. dissertation and sharing discussions.

REFERENCES

1. Crow SC. Stability theory for a pair of trailing vortices. *AIAA Journal* 1970; **8**:2172–2179.
2. Widnall SF, Bliss DB, Tsai CY. The instability of short waves on a vortex ring. *Journal of Fluid Mechanics* 1974; **66**:35–47.
3. Moore DW. Finite amplitude waves on aircraft trailing vortices. *Aeronautical Quarterly* 1972; **23**:307–314.
4. Leonard A. Numerical simulation of interacting, three-dimensional vortex filaments. In: Richtmyer RD (ed.), *Lecture Notes in Physics 35*. Springer-Verlag: New York, 1975; pp. 245–250.
5. Crow SC, Bate ER. Lifespan of trailing vortices in a turbulent atmosphere. *Journal of Aircraft* 1976; **13**: 476–482.
6. Sarpkaya T, Daly JJ. Effect of ambient turbulence on trailing vortices. *Journal of Aircraft* 1987; **240**:399–404.
7. Spalart PR, Wray AA. Initiation of the Crow instability by atmospheric turbulence. Proceedings of Symposium on the Characterization and Modification of Wakes from Lifting Vehicles in Fluids, AGARD-CP-584, 1996.
8. Han J, Lin Y, Schowalter DG, Arya SP, Proctor FH. Large-eddy simulation of aircraft wake vortices: atmospheric turbulence effects. Proceedings of NASA First Wake Vortex Dynamic Spacing Workshop, Hampton, VA, NASA CP-97-206235, 1997; pp. 131–144.
9. Robins RE, Delisi DP. Numerical simulations of three-dimensional trailing vortex evolution. *AIAA Journal* 1997; **35**:1552–1555.
10. Zheng ZC, Baek K. N–S simulations of Crow-type instabilities in vortex wakes. In *37th AIAA Aerospace Sciences Meeting and Exhibit*, January, 1999, Reno, NV, AIAA 99-0981.
11. Thomas PJ, Auerbach D. The observation of the simultaneous development of a long- and short-wave instability mode on a vortex pair. *Journal of Fluid Mechanics* 1994; **265**:289–302.
12. Leweke T, Williamson CHK. Cooperative elliptic instability of a vortex pair. *Journal of Fluid Mechanics* 1998; **360**:85–119.
13. Orlandi P, Carnevale GF, Lele SK, Shariff K. DNS study of stability of trailing vortices. *Proceedings of the Summer Program 1998*, Center for Turbulence Research, 1998; pp. 187–208.
14. Klein R, Majda AJ. An asymptotic theory for the nonlinear instability of antiparallel pairs of vortex filaments. *Physics of Fluids* 1993; **5**:369–379.
15. Shariff K, Verzicco R, Orlandi P. A numerical study of three-dimensional vortex ring instabilities: viscous corrections and early nonlinear stage. *Journal of Fluid Mechanics* 1994; **279**:351–375.
16. Shariff K, Leonard A. Vortex rings. *Annual Review of Fluid Mechanics* 1992; **24**:235–279.
17. Rosenhead L. The spread of vorticity in the wake behind a cylinder. *Proceedings of the Royal Society of London A* 1930; **127**:590–612.
18. Wang HY. A study of short-wave instability on vortex filaments. Ph.D. dissertation, Department of Mathematics, University of California, Berkeley, CA, 1996.
19. Klein R, Knio OM. Asymptotic vorticity structure and numerical simulation of slender vortex filaments. *Journal of Fluid Mechanics* 1995; **294**:275–321.
20. Ashurst WT, Meiburg E. Three-dimensional shear layers via vortex dynamics. *Journal of Fluid Mechanics* 1988; **189**:87–116.
21. Meiburg E. Three-dimensional vortex dynamics simulations. In: Green SI (ed.), *Fluid Vortices*. Kluwer Academic Publishers: The Netherlands, 1995; pp. 651–685.
22. Leonard A. Vortex methods for flow simulation. *Journal of Computational Physics* 1980; **37**:289–335.
23. Lamb H. *Hydrodynamics*, 6th edn. Dover Publications: New York, 1945.
24. Saffman PG. The velocity of viscous vortex rings. *Studies in Applied Mathematics* 1970; **49**:371–380.
25. Thomson Sir W. Vibration of a columnar vortex. *Mathematical and Physical Papers*, Vol. 4. Cambridge University Press: Cambridge, 1910; pp. 152–165.
26. Moore DW, Saffman PG. The motion of a vortex filament with axial flow. *Philosophical Transactions of the Royal Society of London A* 1972; **272**:403–429.
27. Krishnamoorthy V. Vortex breakdown and measurements of pressure fluctuation over slender wings. Ph.D. thesis, Southampton University, 1966.
28. Wang H. Short wave instability on vortex filaments. *Physical Review Letters* 1998; **80**:4665–4668.

